Regional Studies in Marine Science 90 (2025) 104399

Contents lists available at ScienceDirect

Regional Studies in Marine Science

journal homepage: www.elsevier.com/locate/rsma

Seasonal and interannual variability of the oxygen minimum zone in the Gulf of California entrance: Insights from high-resolution coupled physical-biogeochemical modelling

Carlos Alberto Herrera-Becerril[a,b], François Colas[b,c], Joan-Albert Sanchez-Cabeza[d,*], José Martín Hernández-Ayón[e], Vincent Echevin[b], José Gilberto Cardoso-Mohedano[f], Ana Carolina Ruiz-Fernández[d]

[a] Posgrado en Ciencias del Mar y Limnología, Universidad Nacional Autónoma de México, Av. Universidad 3000, Ciudad Universitaria, Coyoacán, Ciudad de México 04510, Mexico
[b] Laboratoire d'Océanographie et du Climat: Expérimentations et Approches Numériques (LOCEAN-IPSL), Sorbonne Université, IRD, CNRS, MNHN, Paris, France
[c] Laboratoire d'Océanographie Physique et Spatiale (LOPS), IRD/UBO/CNRS/Ifremer, IUEM, Plouzané, France
[d] Unidad Académica Mazatlán, Instituto de Ciencias del Mar y Limnología, Universidad Nacional Autónoma de México, Mazatlán, Sinaloa 82040, Mexico
[e] Instituto de Investigaciones Oceanológicas, Universidad Autónoma de Baja California, Carretera Ensenada-Tijuana 3917, Ensenada 22860, Mexico
[f] Estación el Carmen, Instituto de Ciencias del Mar y Limnología, Universidad Nacional Autónoma de México, Carretera Carmen-Puerto Real km. 9.5, Campeche, Ciudad del Carmen 24157, Mexico

ARTICLE INFO

Keywords:
CROCO-PISCES model
Dissolved oxygen
El Niño–La Niña variability
Marine environment
Northeastern tropical Pacific

ABSTRACT

The oxygen minimum zone (OMZ) in the Gulf of California entrance (GCE) is a crucial feature of the northeastern tropical Pacific, significantly influencing regional biogeochemical cycles and marine ecosystems. This study investigates the seasonal and interannual variability of the OMZ upper boundaries using a high-resolution physical-biogeochemical coupled model. The model results are evaluated against satellite observations, Argo profiles, and *in situ* data, demonstrating its capability to capture key dynamical processes, including mesoscale eddies, poleward undercurrents, and coastal-trapped waves (CTWs). The high-resolution CROCO-PISCES model reveals two alternating periods of shoaling and deepening of the OMZ upper boundary in the Gulf of California Entrance, modulated by seasonal mesoscale dynamics and coastal-trapped wave (CTW) propagation. This study provides novel insights into the interannual influence of El Niño Southern Oscillation (ENSO) events on OMZ dynamics, with El Niño driving significant deepening and contraction of the OMZ, and La Niña promoting shoaling and expansion. These variations are linked to changes in mesoscale dynamics, particularly the modulation of anticyclonic circulation at the Gulf's entrance by equatorially forced CTWs associated with ENSO. The study highlights the complex interplay between local and remote oceanographic processes in determining the OMZ variability in the GCE. This research provides insights into the mechanisms driving OMZ dynamics in the Gulf of California and underscores the need for integrated observational and modeling approaches to predict the response of OMZs to ongoing climate variability.

Abbreviations: CROCO, Coastal and Regional Ocean COmmunity model; CTW, Coastal-trapped wave; DO, Dissolved oxygen; ENSO, El Niño-Southern Oscillation; GCE, Gulf of California entrance; JFM, Winter: January-February-March; AMJ, Spring: April-May-June; JAS, Summer: July-August-September; OND, Fall: October-November-December; LFBRY, Low Frequency Boundary forcings; NRMSE, Normalized root mean square error; OMZ, Oxygen Minimum Zone; OMZ-core, Upper limit of the OMZ core DO < 22 μmol L^{-1}; OMZ-top, Upper limit of the OMZ DO < 45 μmol L^{-1}; OSTIA, Operational Sea Surface Temperature and Ice Analysis; PISCES, Pelagic Interactions Scheme for Carbon and Ecosystem Studies; SGC, Southern Gulf of California; SLA, Sea Level Anomaly; SST, Sea Surface Temperature.

[*] Corresponding author.

E-mail addresses: carlos.herrera.becerril@gmail.com (C.A. Herrera-Becerril), francois.colas@ird.fr (F. Colas), jasanchez@cmarl.unam.mx (J.-A. Sanchez-Cabeza), jmartin@uabc.edu.mx (J.M. Hernández-Ayón), vincent.echevin@locean.ipsl.fr (V. Echevin), gcardoso@cmarl.unam.mx (J.G. Cardoso-Mohedano), caro@ola.icmyl.unam.mx (A.C. Ruiz-Fernández).

https://doi.org/10.1016/j.rsma.2025.104399
Received 17 February 2025; Received in revised form 29 July 2025; Accepted 31 July 2025

1. Introduction

Oxygen minimum zones (OMZs) are ocean areas with persistently very low dissolved oxygen (DO) concentrations ($\text{DO} < 45$ μmol L^{-1}; Fernández-Álamo and Färber-Lorda, 2006; Karstensen et al., 2008). They are typically found in the subsurface layer (100–900 m, below the mixed layer) in regions with poor ventilation and high surface primary productivity, which supplies large amounts of organic matter that depletes oxygen in the water column as it is degraded, such as at the eastern boundaries of the tropical oceans (*e.g.*, the eastern tropical Pacific, the eastern tropical Atlantic, and the northern Indian Ocean) (Helly and Levin, 2004; Fernández-Álamo and Färber-Lorda, 2006; Karstensen et al., 2008; Färber-Lorda and Färber-Data, 2023). Although it is estimated that OMZs occupy only 7 % of the total ocean volume, they are highly relevant for the ocean biogeochemical cycles (Paulmier and Ruiz-Pino, 2009). These zones are estimated to contribute ~35 % of net ocean nitrogen loss by denitrification and anammox processes (Devol et al., 2006; Ward et al., 2009) and are responsible for ~30–50 % of the N_2O emission to the atmosphere, an important greenhouse gas (Bange, 2008; McCoy et al., 2023). OMZs significantly influence the ocean's ecosystems, acting as a biological barrier for most aerobic organisms, including most fishes and species of economic interest (Helly and Levin, 2004; Diaz and Rosenberg, 2008; Gallo and Levin, 2016).

The OMZ in the Northeastern Tropical Pacific is among the most intense and extensive globally (Fernández-Álamo and Färber-Lorda, 2006; Karstensen et al., 2008; Stramma et al., 2008). Its spatial extent depends on the dissolved oxygen (DO) threshold used to define it. A threshold of 45 μmol L^{-1} is widely adopted, as it represents a critical limit below which most epipelagic species experience physiological stress, serving as an ecological boundary (Hofmann et al., 2011). Using this threshold, the OMZ extends along the eastern tropical Pacific from the Baja California Peninsula coast (~25 °N) southward to the Ecuador coast (0 °), merging with the Eastern Tropical South Pacific OMZ (Fernández-Álamo and Färber-Lorda, 2006; Paulmier and Ruiz-Pino, 2009). In the Gulf of California, off the Mexican Pacific coast, the OMZ reaches the large islands region (~28 °N) and typically occurs at depths of ~100 to ~600 m (Delgadillo-Hinojosa et al., 2006; Trucco-Pignata et al., 2019). Near the coast, however, it can shoal to ~50 m or even reach coastal waters during wind-driven upwelling events (Márquez-Artavia et al., 2019; Herrera-Becerril et al., 2022).

The OMZ boundaries are delimited by a complex interaction between biochemical processes, such as microbial respiration (Kalvelage et al., 2015; Bretagnon et al., 2018), and dynamical processes, such as ventilation and horizontal advection of oxygenated waters from adjacent waters (Fuenzalida et al., 2009; Brandt et al., 2015). Processes like coastal upwelling, mesoscale eddies, and coastal trapped waves (CTWs) influence the OMZ upper boundary by inducing vertical displacements of the oxygen-rich mixed layer and shoaling or deepening the oxycline (Vergara et al., 2016; Auger et al., 2021; Espinoza-Morriberón et al., 2019). Climate phenomena, such as El Niño Southern Oscillation (ENSO), also influence the interannual variability of the OMZ boundaries, mostly modifying the largescale and mesoscale circulation patterns and therefore, the biochemical processes (Espinoza-Morriberón et al., 2019; Trucco-Pignata et al., 2019).

This study aims to analyze the seasonal and interannual variability of the Oxygen Minimum Zone (OMZ) boundary at the Gulf of California entrance (GCE) and to untangle the dynamic processes driving this variability. To achieve this, we implemented a regional configuration of the coupled hydrodynamical-biogeochemical model CROCO-PISCES (Coastal and Regional Ocean COmmunity model - Pelagic Interactions Scheme for Carbon and Ecosystem Studies) in the Northeastern Tropical Pacific, conducting a 13-year simulation (2008–2020) and a sensitivity analysis to remote forcings. This is the first time a physical-biogeochemical coupled model, like CROCO-PISCES, is used to study the seasonal and interannual variability of the OMZ boundary in the Gulf of California.

2. Study area

The Gulf of California entrance (GCE) is the zone delimited by the virtual lines between the tip of the Baja California Peninsula (Cabo San Lucas) to El Dorado, Sinaloa (~24 °N on the mainland side; the mouth line) and from Cabo San Lucas to Cabo Corrientes (~20.5 °N) (Lavín and Marinone, 2003). This region is a complex transition zone where different currents and water masses converge. In the surface layer, ramifications of the cold and low-salinity California Current Water (Table 1) reach the area mainly in winter and spring, interacting with the warm and high-salinity Gulf of California Water and the warm and low-salinity Tropical Surface Water. In the subsurface, the nutrient-rich, oxygen-depleted, and saltier Subtropical Subsurface Water overlays, enriched with nutrients, and the colder, oxygen-depleted Pacific Intermediate Water (Lavín and Marinone, 2003; Portela et al., 2016; Trucco-Pignata et al., 2019).

This area is characterized by several dynamic processes that could influence the OMZ boundary. On the continental side of the GC, the occurrence of wind-driven coastal upwelling, mainly from fall to spring, shoals the thermocline/pycnocline and could raise the upper boundary of the OMZ, primarily near the coast (Herrera-Cervantes et al., 2007). This area is also influenced by the generation and propagation of mesoscale eddies, particularly near the Cabo San Lucas (23 °N) and Cabo Corrientes (20 °N) capes (Fig. 1), which are hotspots for eddy formation due to the interaction between currents and coastal irregularities (Kurczyn et al., 2012). Along the coast, the poleward propagation of CTWs modulates the depth of the pycnocline and could also induce vertical displacements of the oxycline (Gutiérrez et al., 2014). These CTWs typically originate from the equatorial region; however, wind gaps from the gulfs of Tehuantepec, Papagayo (Costa Rica), and Panama could also generate them (Spillane et al., 1987; Flores-Vidal et al., 2014). From Cabo Corrientes, some of the CTWs continue along the coast inside the GC, while others can pass the Baja California peninsula tip and continue their poleward propagation along the outer side of the peninsula (Gómez-Valdivia et al., 2015). In the subsurface, the Mexican Coastal Current (MCC) flows poleward along the coast between Gulf of Tehuantepec (14 °N) and Gulf of California (~24 °N), mainly during spring and fall, when it is enhanced by the semiannual CTWs (Gómez-Valdivia et al., 2015). This poleward flux could advect oxygen-depleted Subtropical Subsurface Water toward the GCE.

The interannual variability in the Southern Gulf of California (SGC) is strongly influenced by ENSO, especially during winter, due to its connection to the Equatorial Pacific by the CTWs corridor along the continental border and atmospheric teleconnections (Lavín and Marinone, 2003; Herrera-Cervantes et al., 2007; Sanchez-Cabeza et al., 2022). During La Niña phases, the main seasonal patterns are enhanced: upwelling-favorable winds are intensified, and the thermocline is shoaled, resulting in cooler, nutrient-rich waters near the coast. In

Table 1
Water masses in the Gulf of California; CCW: California Current Water, TSW: Tropical Surface Water, GCW: Gulf of California Water, StSsW: Subtropical Subsurface Water, PIW: Pacific Intermediate Water, PDW: Pacific Deep Water. DO classification: oxygen-rich (>90 μmol L^{-1}), oxygen-poor (45–90 μmol L^{-1}), oxygen-depleted (<45 μmol L^{-1}).

Water mass	Θ (°C)	Salinity (g kg^{-1})	Depth (m)	DO level
CCW	10–21	< 34.6	0–150	Oxygen-rich
TSW	> 25.1	< 34.6	0–50	Oxygen-rich
GCW	> 12	> 35.1	0–150	Oxygen-poor - Oxygen-rich
StSsW	9–18	34.6–35.1	45–520	Oxygen-depleted
PIW	4–9	34.6–34.9	400–1000	Oxygen-depleted
PDW	< 4	> 34.5	> 1000	Oxygen-poor

Modified from Portela et al. (2016), updated with data from Trucco-Pignata et al. (2019).

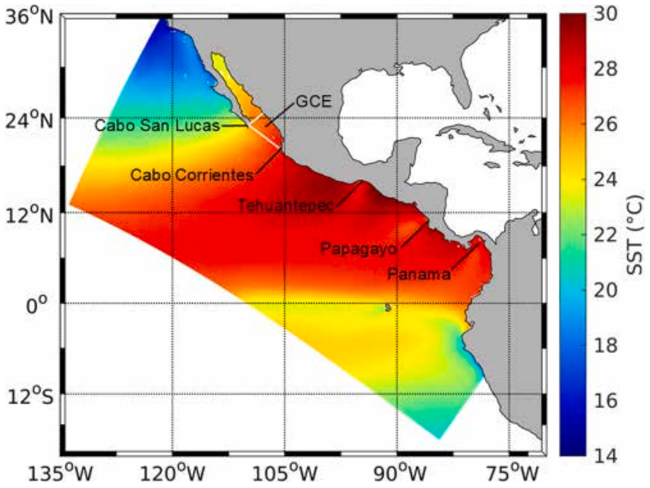

Fig. 1. Domain of the model, with mean CROCO SST calculated over the 2010–2020 period. White lines denote the Gulf of California entrance (GCE).

contrast, during El Niño phases, the relaxation of upwelling-favorable winds deepens the thermocline, bringing warmer, nutrient-poor waters to the surface and reducing biological productivity (Herrera-Cervantes, 2007; Lluch-Cota et al., 2010; Páez-Osuna et al., 2016).

3. Methods

3.1. *The physical-biogeochemical coupled model CROCO-PISCES*

The Coastal and Regional Ocean Community model (CROCO; Hilt et al., 2020) was used to study the hydrodynamics in the Northeastern Tropical Pacific. CROCO solves the Primitive Equations based on the Boussinesq and hydrostatic approximations built upon the former ROMS kernel (Shchepetkin and McWilliams, 2005; Penven et al., 2006). It uses stretched terrain-following sigma vertical coordinates and an Arakawa-C horizontal grid. Horizontal advection of temperature and salinity is calculated using the Rotated and Split 3rd-Order Upstream Biased Advection Scheme (RSUP3; Lemarié et al., 2012). Vertical mixing is parameterized using KPP parameterization (Large et al., 1994). For a detailed model description, the reader is referred to Shchepetkin and McWilliams (2005) and, (2009).

The hydrodynamical model CROCO was coupled with the PISCES biogeochemical model (Pelagic Interaction Scheme for Carbon and Ecosystem Studies). PISCES simulates the marine biogeochemical cycles of carbon, nutrients (NO_3^-, PO_4^{3-}, Si, and Fe), and dissolved oxygen (DO). PISCES has four living compartments split into two size classes (nanophytoplankton and diatoms, and microzooplankton and mesozooplankton, respectively) and three non-living compartments (semi-labile dissolved organic matter, small sinking particles, and large sinking particles) (Aumont and Bopp, 2006; Aumont et al., 2015). We used the default model parameters as detailed by Aumont et al. (2015).

CROCO-PISCES computes the oxygen evolution considering dynamical transport, biogeochemical processes (sources and sinks), and air-sea exchange. Dynamical transport considers horizontal and vertical advection, as well as vertical mixing. The biogeochemical processes include oxygen production by photosynthesis, consumption by dissolved organic matter remineralization, microzooplankton and mesozooplankton respiration, and nitrification (Aumont et al., 2015; see also Resplandy et al., 2012 and Espinoza-Morriberón et al., 2019). Our particular model configuration is described in Section 3.2. Data used to force the model at the surface boundary and the oceanic lateral open boundaries are described, respectively, in Section 3.3 Atmospheric forcings, and Section 3.4 Open boundary conditions. All the information is also summarized in Table 2. In this work, as a first approach to untangle the OMZ variability in the GC, we focus on oxygen variability driven by the physical processes (particularly advection) rather than the biogeochemical processes and air-sea exchange. The omission of biogeochemical analysis limits a comprehensive understanding of OMZ variability and will be addressed in future studies.

3.2. *Model configuration*

We used a rotated rectangular grid to minimize land points and align the right boundary with the continental margin. The model domain extends from 13 °N, 134 °W in the northern left corner to 18 °S, 84 °W in the southern left corner, and 36 °N, 121 °W in the northern right corner, in front of California, to 10 °S, 78 °W in the southern right corner, in

Table 2
Summary of the different datasets used in the paper, with their original spatial and temporal resolution.

Name	Variables	Spatial coverage & resolution	Temporal resolution	Use	Reference
ETOPO2	Bottom topography	Global coverage, 0.033°	NA	Model configuration	Smith and Sandwell, (1997)
ERA5	10 m wind speed, air surface temperature, specific humidity, precipitation rate, and shortwave, longwave downward radiation	Global, 0.25°	Hourly	Model atmospheric forcings	Hersbach et al., (2018)
Fe deposition	Fe atmospheric deposition	Global, 1°	Monthly climatological means	Model atmospheric forcings	Tegen and Fung, (1995)
Mercator Ocean reanalysis (GLOBAL MULTIYEAR PHY 001 030)	Temperature, salinity, sea surface height, and velocity components	Global, 1/12°	Daily	Initial and open ocean boundary conditions for the dynamical model	CMEMS, 2023
WOA 2009	DO, NO_3, PO_4, SiO_3	Global, 1°	Monthly climatological means	Initial and open boundary conditions for the biogeochemical model	Boyer et al., (2009)
Climatology of Global PISCES simulation	Total alkalinity, dissolved iron	Global 2°	Monthly climatological means	Initial and open boundary conditions for the biogeochemical model	Aumont et al., (2015)
OSTIA	Sea surface temperature (SST)	Global, 0.05°	Daily	Model validation	Good et al., (2020)
AVISO+	Sea level anomaly (SLA)	Global, 0.25°	Daily	Model validation	Pujol et al., (2016)
ARGO biogeochemical floats	DO and temperature profiles	Punctual profiles	Punctual profiles	Model validation	Claustre et al., (2020)
CRUISE data	DO and temperature	Punctual profiles along the GC	Punctual profiles from 3rd to 16th of June 2015	Model validation	Trucco-Pignata et al., (2019)

front of Peru (Fig. 1). Since the equatorially-forced CTWs highly influences the Northeastern Tropical Pacific (Spillane et al., 1987), the domain's southern limit was chosen to include the continental border of the Pacific at the equator. The horizontal grid resolution was ~9 km, and the vertical discretization had 45 sigma layers, with finer resolution towards the surface. The bottom topography was interpolated from ETOPO2 (Earth TOPOgraphy: Smith and Sandwell, 1997) and smoothed to avoid potential errors in the pressure gradient (Shchepetkin and McWilliams, 2005).

3.3. Atmospheric forcings

We used the COARE3.0 (Coupled Ocean-Atmosphere Response Experiment) bulk formulation (Fairall et al., 2003) to compute the wind stress and heat fluxes imposed at the air-sea interface of the dynamical model. The 10 m wind speed components, surface air temperature, specific humidity, precipitation rate, and shortwave and longwave downward radiation were obtained from ERA5 reanalysis hourly products at 0.25 ° resolution (Hersbach et al., 2018), then averaged to daily means and interpolated onto the model grid. The Fe atmospheric deposition required for the PISCES model's surface forcing was calculated from Tegen and Fung's model results (1995), assuming constant values for iron content and solubility.

3.4. Open boundary conditions

The open ocean boundary conditions for the dynamical model (temperature, salinity, sea surface height, and velocity components) were obtained from the Mercator Ocean reanalysis (1/12°, daily products) (GLOBAL_MULTIYEAR_PHY_001_030), then averaged every five days and interpolated into the model boundaries grid (CMEMS, 2023).

The initial and open boundary conditions for the biogeochemical model were sourced from multiple datasets. DO and macronutrients (NO_3, PO_4, SiO_3) were obtained from the World Ocean Atlas 2009 (WOA 2009, 1° resolution; Boyer et al., 2009). Dissolved inorganic and organic carbon were derived from the Global Ocean Data Analysis Project (GLODAP, 1° resolution; Key et al., 2004). Total alkalinity and dissolved iron concentrations were taken from the climatology of a global PISCES simulation (2° resolution; Aumont et al., 2015). The surface forcings, initial conditions, and boundary conditions were preprocessed using the CROCOTOOLS package (Penven et al., 2019).

3.5. Model simulations

We performed a 13-year control simulation (2008–2020). The spin-up was accomplished by repeating the year 2008 three times to reach a steady state, then the output was used as the initial condition (1 January 2008) for the control simulation. Model variables (outputs) were stored as five-day averages. To include an equal number of El Niño and La Niña events, the first two years (2008–2009) were discarded, and the analyses were performed from 2010 to 2020. This period includes El Niño periods 2014–2016 and 2018–2019, and La Niña periods 2010–2012 and 2016–2018.

To analyze the influence of remote oceanic forcings, particularly the equatorially-forced CTWs, on mesoscale dynamics and the OMZ boundary variability, we performed a sensitivity experiment. This involved running a simulation (named LFBRY) in which the ocean boundary forcings are yearly averages. The objective was to filter out seasonal and intra-seasonal variability while preserving the low-frequency interannual signal.

3.6. Model's performance evaluation

To evaluate the model's performance, the model results were compared with observations from different data sources (Table 2). The mean state was evaluated by comparing the modeled annual and seasonal means of the sea surface temperature (SST) over the 2010–2020 period with the observed SST means from Operational Sea Surface Temperature and Ice Analysis (OSTIA) (Good et al., 2020). To evaluate the interannual performance, we compared modeled and observed (OSTIA) SST monthly anomaly time series averaged in the southern GC (Fig. S1). We also compared modeled and observed sea level anomaly (SLA) time series averaged in the same area (Fig. S2).

The model skill is a normalized metric that quantifies the agreement between model results and observations, ranging from 0 (no agreement) to 1 (perfect agreement) (Willmott, 1981). It is calculated as one minus the normalized sum of squared differences between model outputs and observations. We estimated the model skill and the root mean square error normalized to the range of model values (NRMSE) for both monthly anomaly SST and SLA, time series comparison.To evaluate the mesoscale activity, we calculated the standard deviation of the 95-day high-passed sea level anomaly (henceforth named SLA standard deviation) during the 2010–2019 period. We compared it to the SLA standard deviation obtained from the AVISO (Archiving, Validation and Interpretation of Satellite Oceanographic data) satellite altimetry data, following the methodology from Liang et al. (2012).

To evaluate the modeled vertical structure, we compared the temperature and DO profiles from biogeochemical-ARGO floats (Claustre et al., 2020) with profiles from the nearest model grid at the same time. This analysis included 632 profiles from biogeochemical-ARGO floats. Since no biogeochemical ARGO floats were available in the GC during the simulation time period, we also compared the model temperature and DO with a transect along the GC sampled in June 2015 (Trucco-Pignata et al., 2019).

4. Results

4.1. Model evaluation

The SST annual mean comparison with OSTIA revealed a widespread cold bias of −0.2 to −0.5 °C across most of the domain, with a larger bias (up to 1.2 °C) in areas near the northern and southern continental borders (Fig. S1A). Seasonally, the comparison for winter (JFM) showed a cold bias [−0.5 to −1 °C] over much of the study area, but a notable positive (warm) bias within the GC itself. This warm bias ranged from [0–1 °C] in the SGC to [0.7–2 °C] in the northern GC (Fig. S1B). In contrast, the summer (JAS) comparison revealed a moderate warm bias of ~0.5 °C around the GCE and a slight cool bias [−0.1 to −0.3 °C] in the southern GC (Fig. S1C).

These spatial and temporal patterns in SST bias may have some implications for the modeled ocean structure. The warm bias within the GC during winter would induce a modeled thermocline deeper than observed, which would affect the ventilation of subsurface waters and the vertical transport of oxygen. Despite these biases, the model successfully reproduced the interannual SST variability, with a skill of 0.97 and an NRMSE of 0.06, and correctly captured the strong anomalies associated with El Niño and La Niña events.

The model adequately captured the range of intra-seasonal and interannual SST variations (Fig. S2). The model's skill score for the SST monthly anomalies below 28°N was 0.97, and the NRMSE was 0.06, indicating a very satisfactory level of performance. The pronounced cold anomalies in 2010 and 2011, as well as the warm anomalies in 2014 and 2015 associated with La Niña and El Niño events, were also accurately reproduced.

The SLA standard deviation comparison (Fig. 2) showed that the model's mesoscale variability is slightly lower than that derived from AVISO. However, the model reproduces well the areas with enhanced mesoscale activity, such as around Cabo Corrientes and South of Cabo San Lucas (21°-23°N and 112°-108°W; Fig. 1) (Kurczyn et al., 2012). The SLA time series comparison between the model and AVISO in the south GC showed a model skill was 0.96 and an NRMSE of 0.08 (Fig. S3).

Model validation of DO is constrained by the limited availability of in

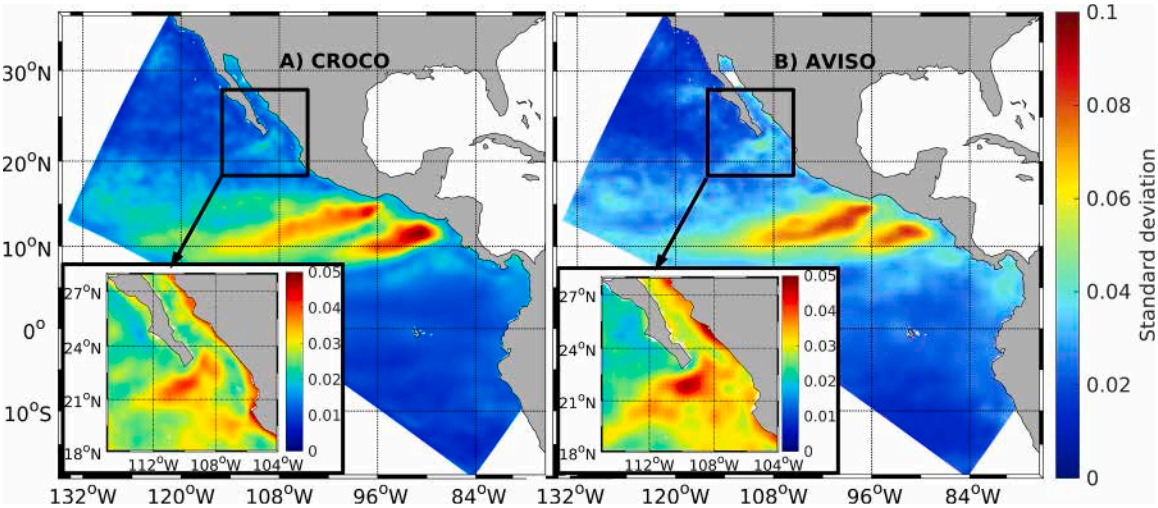

Fig. 2. Standard deviation from 95-day high-passed sea level anomaly (SLA-SD) from A) CROCO and B) AVISO altimetry data (2010–2019).

situ oxygen measurements in the GCE, which relies primarily on sparse ARGO profiles and June 2015 cruise data, thereby restricting the assessment of fine-scale variability, particularly in coastal regions. The comparison with ARGO profiles showed that the model was able to estimate the thermocline depth correctly albeit slightly more diffusive (Fig. 3B). The modelled and observed oxyclines were of similar intensity (~4 μmol L^{-1} m^{-1}) but deeper in the model (Fig. 3A). The mean difference of the oxycline depth (depth difference for each DO from 20 to 200 μmol L^{-1}) between selected CROCO and ARGO profiles was 17.1 ± 0.1 m. The NRMSE for the CROCO profiles compared to ARGO from surface to 250 m depth was 0.17 for DO and 0.08 for temperature.

The comparison of the modelled DO and temperature with the June 2015 transect along the GC (Trucco-Pignata et al., 2019), confirmed that the modelled oxycline was somewhat deeper and more diffuse than the observed, but reproduced well some of the observed latitudinal patterns of temperature and the upper limit of the OMZ (44 μmol L^{-1}), particularly the front around 24 °N (Figs. S4 & S5).

In the following, we explore the variability of the OMZ in the GCE and discuss the processes responsible for it based on the model results. The impact of the afore-mentioned DO bias is discussed in the last section.

4.2. Seasonal variability

Several DO thresholds have been used to define the OMZ boundaries according to different criteria. Here, we use the 44 μmol L^{-1} DO concentration to define the upper limit of the OMZ, referred to hereafter as OMZ-top. A similar threshold (44 μmol L^{-1}) has been used in previous studies in the same zone (Sánchez-Velasco et al., 2017; Trucco-Pignata et al., 2019; Sánchez-Pérez et al., 2021). We also used the 22 μmol L^{-1} isopleth, also reported as the "severe hypoxia" threshold, to identify the OMZ core in the model results, hereafter referred as OMZ-core (Helly and Levin, 2004; Diaz and Rosenberg, 2008; Hofmann et al., 2011; Färber-Lorda and Färber-Data, 2023).

In the Mexican Pacific coast, the OMZ-top is shallower (<100 m) next to the coast up to Cabo Corrientes (Fig. 4), then it deepens to the north along the GC up to ~250 m depth around 28 °N, at the south of the large islands. The major seasonal variation of the OMZ-top occurs next to the continental border on the mainland side of the GC (Fig. 4). To visualize the OMZ boundary variability (OMZ-top and OMZ-core) along the continental border, we defined a transect along the 500 m isobath next to the mainland coast (Fig. 4C) and plotted the DO mean concentration over the 2010–2020 period (Fig. 5) and the monthly means

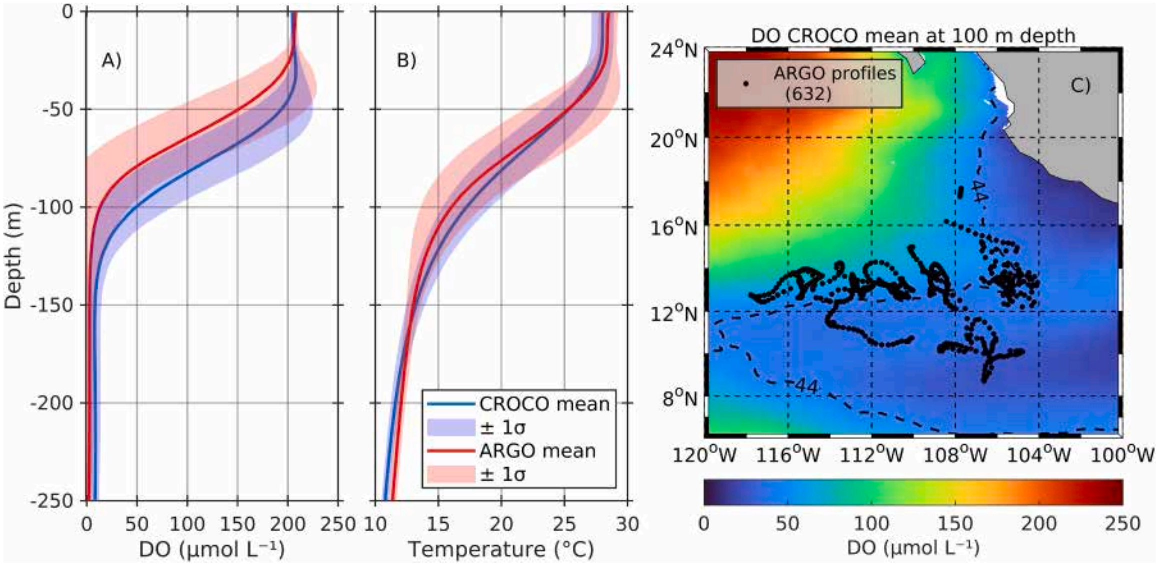

Fig. 3. Comparison of the CROCO model results with ARGO floats. A) Dissolved oxygen (DO) and B) temperature means from all available profiles. C) Map with the location of ARGO profiles and DO from the model at 100 m depth. The dashed line remarks the limits of oxygen minimum zone (OMZ) (44 μmol L^{-1}) at that depth.

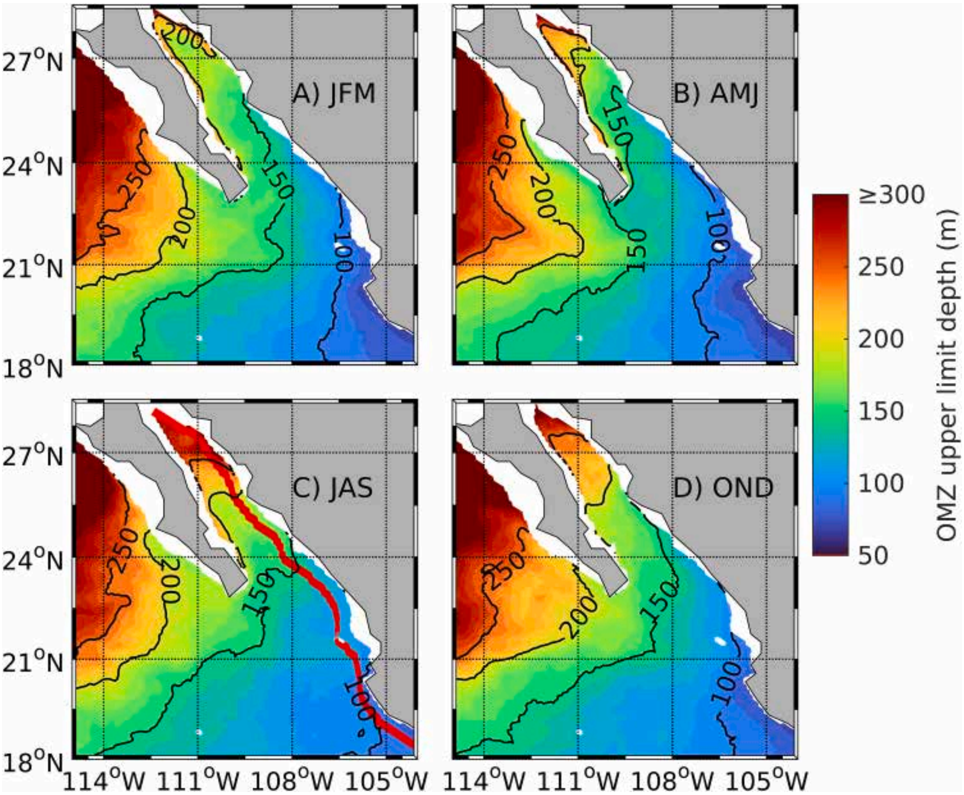

Fig. 4. Seasonal means of the depth of the OMZ upper limit (DO = 44 μmol L^{-1}) during the 2010–2020 period: A) January-February-March, B) April-May-June, C) July-August-September, and D) October-November-December. The red line along the Gulf of California in C) shows the position 500 m isobath selected to draw the vertical section in Fig. 5.

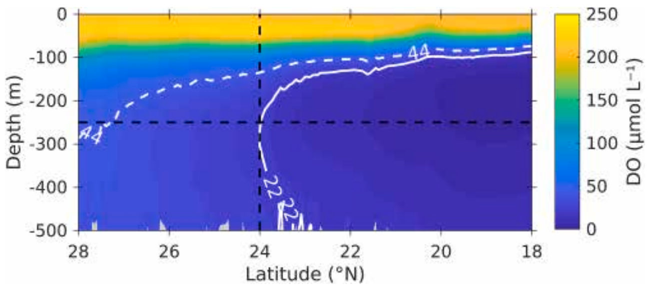

Fig. 5. Mean of dissolved oxygen (DO) concentration, over the 2010–2020 period, along a vertical section following the 500 m isobath in the continental side of the Gulf of California, (Fig. 4C). Dashed line marks the 44 μmol L^{-1} isopleth (OMZ-top), and continuous line marks the 22 μmol L^{-1} isopleth (OMZ-core). The horizontal dashed line marks the 250 m depth, and the vertical line at 24 °N denotes where this transect crosses the Gulf of California mouth.

(Fig. S6).

The monthly means of the OMZ-top and OMZ-core along the 500 m isobath transect revealed a semiannual pattern of two alternating periods of shoaling and deepening of the OMZ-top and poleward expansion and contraction of the OMZ-core (Fig. S6). The first shoaling/expansion period occurs from October to January and reaches its maximum in December. During this period, the OMZ-top shoals along the coast, between ~20.5 °N (Cabo Corrientes) and ~25 °N (Topolobampo) (Fig. 4D), and the OMZ-core extends northward, reaching its seasonal maximum position (~24.75 °N). Later in winter (February and March), the model shows a weak deepening of the OMZ-top and contraction of the OMZ-core to the south, just around the GC mouth. During spring (April-May), the model shows a second and strongest period of shoaling and poleward expansion of the OMZ boundary, with a maximum in May. In this period, the OMZ-top is shallowest, and the OMZ-core reaches its northernmost position (~25 °N).

In summer (JAS), the model shows a second and the most intense period of southward contraction, when the OMZ-top is progressively deepened to the north of ~27 °N, where it abruptly sinks from ~200 m to ~400 m, creating a front-like pattern. Unlike during other seasons, the summer deepening of the OMZ-top occurs rather homogeneously across the gulf width around the GC mouth (Fig. 4C). In summer, the OMZ-core rapidly contracts to the south; from July, the OMZ-core is positioned outside of the GC and reaches its southernmost position in September (~23 °N; Fig. S6). Fig. 6 summarizes this seasonal cycle by showing the monthly means of the OMZ-top at the GC mouth latitude (24 °N) in the alongshore transect (Fig. 5) and the OMZ-core northernmost position reached along the same transect. Intraseasonal CTWs had a weak impact on the variability of the OMZ boundary position, as the LFBRY simulation showed similar results to the control simulation albeit smoother transitions in the range variation of OMZ-top depth and OMZ-core northern position, particularly during the summer contraction (Fig. 6A&B).

4.3. *Interannual variability*

To compare the influence of El Niño/La Niña events on the OMZ boundary, we calculated seasonal means of the OMZ-top and OMZ-core position during La Niña 2010–2011 and El Niño 2015–2016, both of which were strong events (Sanchez-Cabeza et al., 2022; Boening et al., 2012). During La Niña, the OMZ-top was ~50 m shallower than average in almost all the SGC (Fig. 7A,C & 8B), and the alongshore OMZ-core was slightly shallower than the climatology, reaching a position around one degree further north (Fig. 8B).

In contrast, during El Niño 2015–16, the OMZ deepened in the GC. During fall (OND-2015), the OMZ-top was deeper than the average

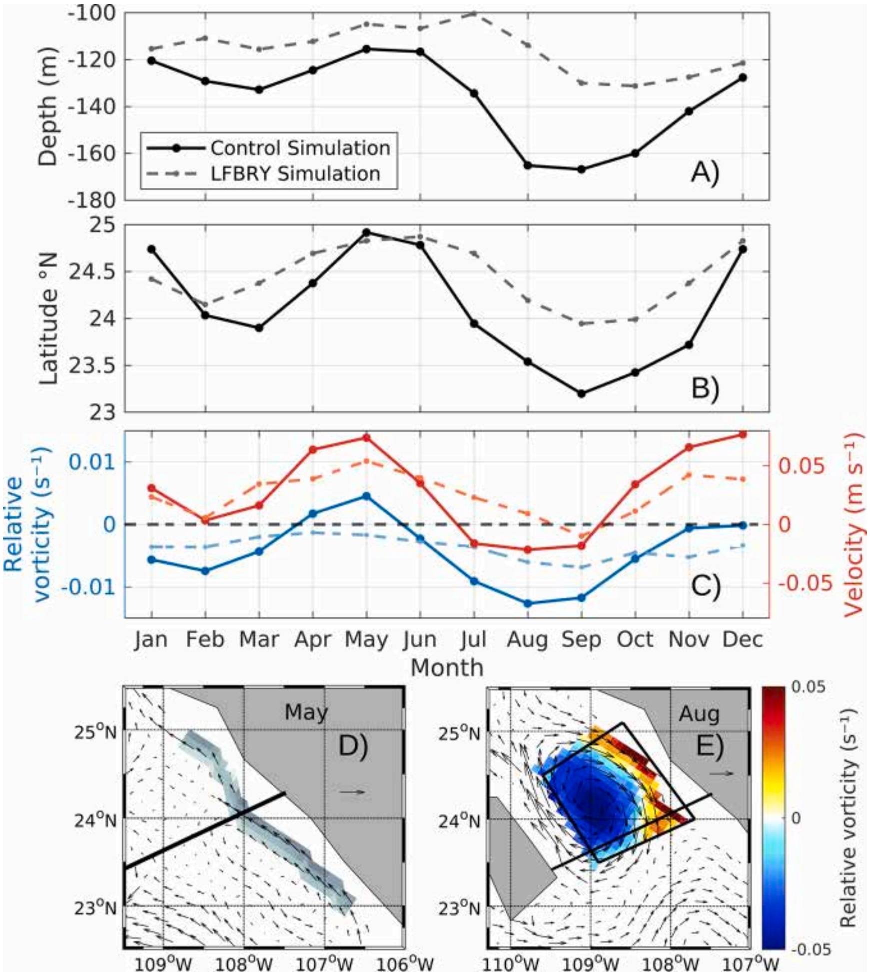

Fig. 6. Seasonal cycle of A) mean depth of OMZ-top (DO = 44 µmol L^{-1}) at 24 °N in the transect along the coast in Fig. 5. B) Seasonal cycle of the northernmost position reached by the OMZ-core (DO = 22 µmol L^{-1}) at 250 m in the same transect. C) Relative vorticity (blue) in the area inside the box in E), and mean velocity (red) in the transect along the coast in D).

(Fig. 7B,D & 8 A). In winter (JFM-2016), the OMZ-top was deeper, and the OMZ-core showed a marked deviation from the seasonal mean, being positioned in a front-like pattern, out of the GC mouth, southern than 22 °N (Fig. 8B).

CTWs are one of the mechanisms through which the ENSO signal is propagated from the Equatorial Pacific to the CG, and its passage can be observed as anomalies of sea level. The Hovmöller plot of the SLA and OMZ-top anomalies along the 200 m isobath next to the Mexican Pacific (Fig. 9D) coast shows two periods of positive (downwelling) and negative (upwelling) anomalies in both variables, which coincides with El Niño 2015–16 and La Niña 2010–11 events (Fig. 9A,B). The SLA anomalies showed a continuous pattern along all the transect, which suggests that the CTWs propagate along the Mexican Pacific coast. In contrast, the OMZ-top anomalies are more diffuse, particularly at the north of 22 °N (Fig. 9A). To analyze the influence of the CTWs in the OMZ-top variability, we calculated the cross-spectrum of SLA and OMZ-top anomalies in different points south (19 °N) and north (23 °N) of Cabo Corrientes (see Fig. 9D). This cross-spectrum showed a peak of shared energy near ~55 days at 19 °N. Still, the peak did not exist at 23 °N. Expectedly, the peaks were not observed in the spectrums from the LFBRY simulation (Fig. 9E).

5. Discussion

Our model simulation adequately captured the seasonal and intraseasonal variability of physical variables (SST and Sea Surface Height), suggesting that the main dynamical processes are correctly simulated (Figs 2, S1, S2 & S3). However, as the model estimated a deeper oxycline than observations (Figs. 3, S4), the exact position of the OMZ-top and the OMZ-core is expected to be shallower than simulated. Our simulation also reproduced well the latitudinal variations of the OMZ boundary (Figs. S4 & S5) and can thus be useful in studying the dynamical processes driving these variations, as abundant observations are not abundant in the region. In fact, to date, not a single biogeochemical ARGO float with available oxygen measurements has been deployed in the GC, and the World Ocean Atlas climatology of DO includes very few observations in the region (Garcia et al., 2024).

The scarcity of in situ measurements, particularly for dissolved oxygen, poses a significant limitation for validating the CROCO-PISCES model in the GCE. The absence of biogeochemical ARGO floats and the reliance on sparse cruise data (e.g., June 2015; Trucco-Pignata et al., 2019) restrict our ability to fully assess the model's performance, especially for fine-scale spatial and temporal OMZ variability. The lack of dense observational data hinders precise bias attribution and parameter tuning, potentially underestimating the ecological impacts of hypoxic conditions, such as biological stress on epipelagic species (Hofmann et al., 2011). Despite these challenges, the model captures large-scale OMZ patterns, including semiannual cycles and latitudinal gradients (Figs. 5, S4), validated against available data. Future work should prioritize the deployment of biogeochemical ARGO floats and conducting targeted cruises to enhance validation, alongside higher-resolution simulations to better resolve coastal dynamics.

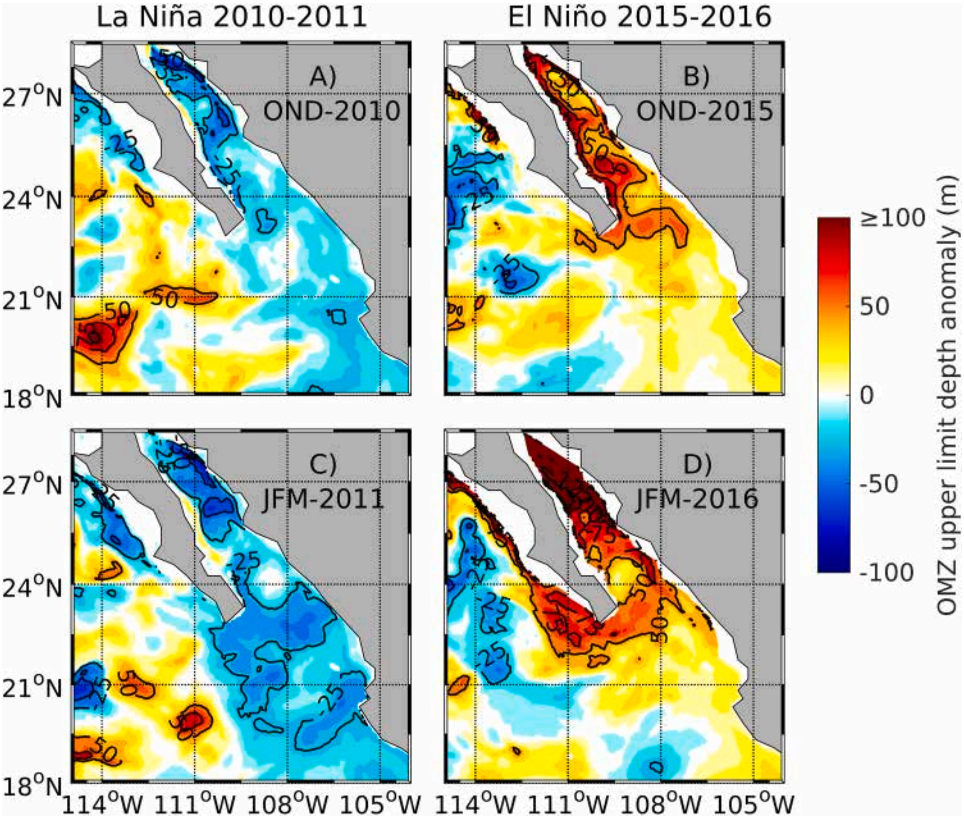

Fig. 7. Comparison of the OMZ upper limit (DO = 44 μmol L^{-1}) depth anomaly between La Niña 2010–2011 (left column: a,c) and El Niño 2015–2016 (right column: b,d) during fall and winter.

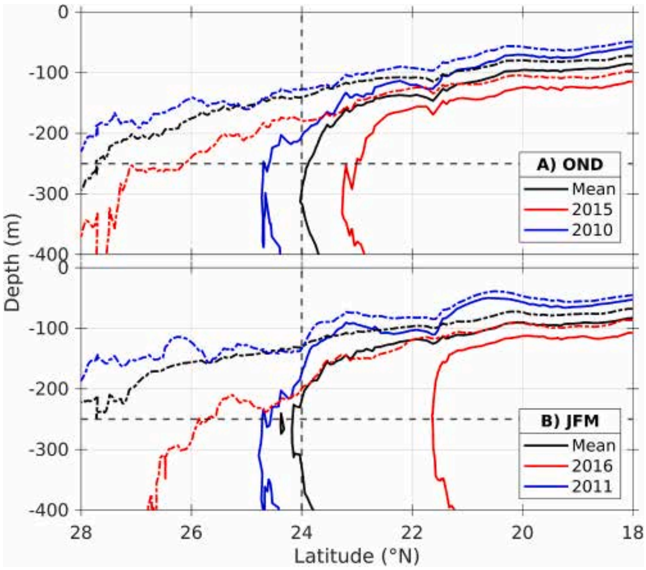

Fig. 8. Quarterly means of the position of the OMZ-top (DO = 44 μmol L^{-1}, dashed line) and OMZ-core (DO = 22 μmol L^{-1}, continuous line) along the 500 m isobath transect (shown in Fig. 4) in A) fall (OND) and B) winter (JFM), during El Niño 2015–16 (red line) and La Niña 2010–11 (blue line).

5.1. Transition area and decoupling

The OMZ-top and the OMZ-core have similar temporal variability but different spatial behavior along the GCE and SGC. Cabo Corrientes acts as a tipping point where the transition area starts. To the south of the cape, the isopleths are close while to the North the isopleths decouple: the OMZ-top remains visible along all the SGC, up to the large islands, while the OMZ-core rapidly deepens, creating a front-like pattern at depths from ~150 to ~400 m, with a latitudinal variability around the GC mouth (from ~23–25 °N) (Fig. 5&S6). A similar decoupling pattern has been observed by Cepeda-Morales et al. (2013) in a transect perpendicular to the coast at the Cabo Corrientes latitude. This decoupling could be a characteristic of a transitional area.

5.2. Influence of poleward undercurrent

The seasonal variability of the OMZ boundary along the continental side of the GCE is mainly related to subsurface circulation patterns, particularly with the alternated periods of semiannual poleward undercurrent occurring in fall and spring and the formation of an anticyclonic eddy in the GC mouth during winter and summer (Fig. 10) (Kessler, 2006; Zamudio et al., 2008; Godínez et al., 2010; Gómez-Valdivia et al., 2015). In the GCE, the poleward undercurrent, which is part of the Mexican Coastal Current flows in a narrow strip along the continental slope from October to January (fall) and from April to June (spring) (Fig. 10). It has a maximum velocity of ~0.1 m s^{-1} at depths from ~100 m to ~400 m, approximately in the same depth range of the Subtropical Subsurface Water is found (Lavín et al., 2013) (Fig. 11). This flows advects low DO waters from the OMZ northward, pushing the OMZ-core inside the GC, and shoaling of the OMZ-top. The months of maximum poleward flow, December and May, coincide with the northernmost position reached by the OMZ-core, up to ~25 °N along the coast (see Fig. 6B).

5.3. Influence of an anticyclonic eddy at the GC mouth

Approximately one month after each poleward flow peaks, an anticyclonic eddy begins to form in the SGC, as part of an eddy train formed

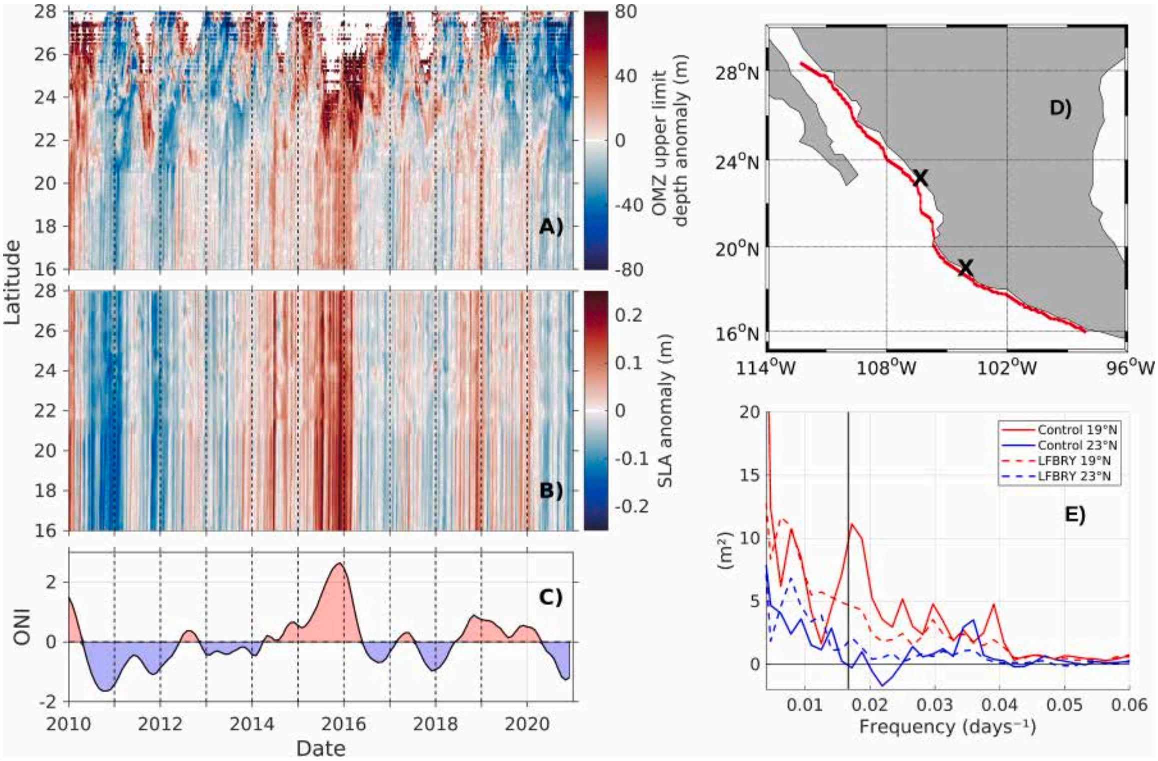

Fig. 9. Hovmöller plots of the A) OMZ upper boundary anomaly and B) sea level anomaly (SLA) along a transect following the 200 m isobath along the Mexican Pacific coast, and C) the Oceanic Niño Index (ONI) time series. D) Transect along the 200 m isobath; X marks show the 19 and 23 °N locations, where the SLA and OMZ top anomalies time series were extracted to calculate the cross-spectra (E). The masked values in the upper panel (A) correspond to strong positive anomalies when OMZ-top is no longer defined (DO is larger than 44 μmol L^{-1} over the entire water column).

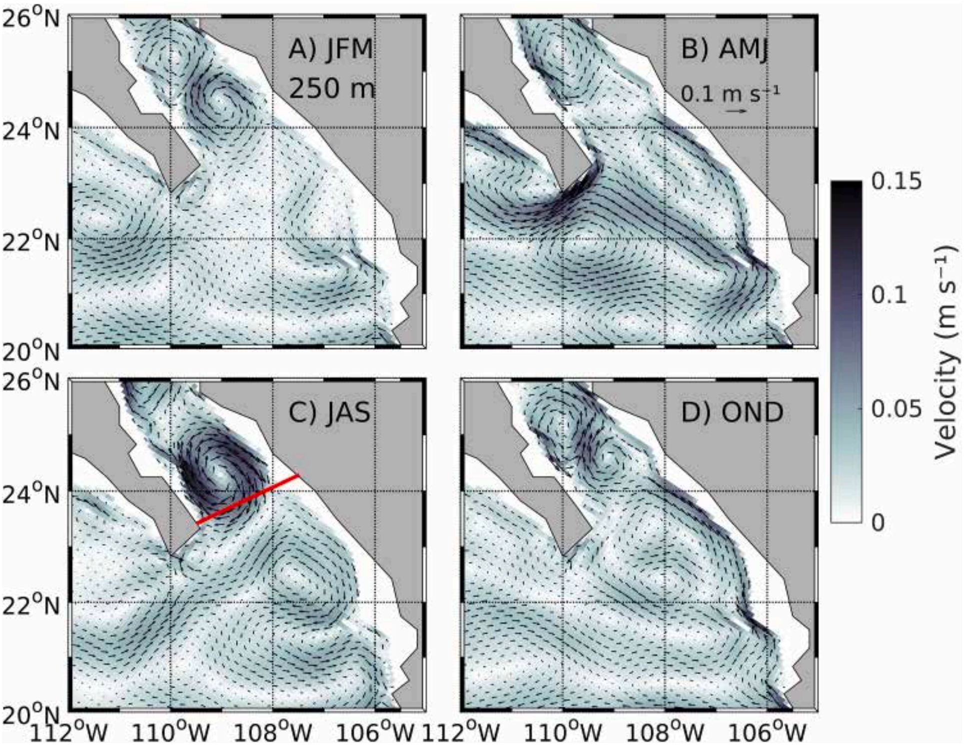

Fig. 10. Seasonal means of velocity at 250 m depth during 2010–2020. The red line in C) shows the position of the transect across the GC mouth used in Fig. 11 & 12.

along the GC axis (Fig. 10). This eddy is particularly intense in summer (Fig. 10C). It extends up to 700 m depth, and the difference in its properties (salinity, temperature, and DO) is more delimited in the subsurface (~300 m). Its maximum velocities (up to ~0.14 m s^{-1}) are found from 200 to 600 m during August-September (Pegau et al., 2002; Zamudio et al., 2008; Lavín et al., 2013). Our model results agree with

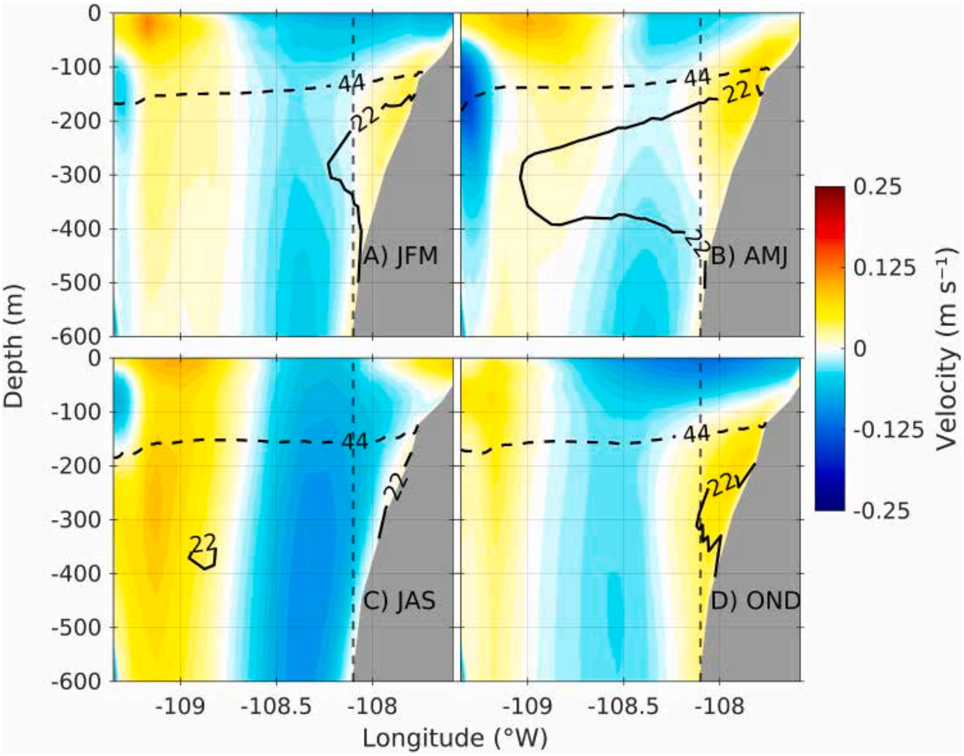

Fig. 11. Seasonal means of velocity perpendicular to the transect across the GC mouth (Fig. 10C). The positive (negative) values indicate poleward (equatorward) flow, the dashed line shows the DO = 44 μmol L^{-1} isopleth, and the continuous line shows the DO = 22 μmol L^{-1} isopleth.

these observations (Fig. 11C). It has been proposed that the eddy train is formed by baroclinic instabilities caused by the interaction of the poleward undercurrent, intensified by the passage of CTWs, with topographic irregularities (Zamudio et al., 2008). Since the poleward flow is stronger in spring than in fall, this hypothesis is consistent with the more intense anticyclonic eddy formed in the GC in late summer than that formed in winter (Fig. 10A&C). It has also been suggested that some eddies in the south of GC could be formed by localized wind impulses and by instabilities caused by the interaction between currents (Lavín et al., 2009; Pantoja et al., 2012). The results of our sensitivity experiment with filtered remote forcing (LFBRY) showed that a much weaker summer eddy is also formed in the absence of intra-seasonal equatorially-forced CTWs (Fig. S7). This supports the hypothesis that CTWs enhance the poleward flow and intensify the eddy train but are not crucial to its formation (Zamudio et al., 2008).

The position of the anticyclonic eddy, close to the GC mouth, provokes a subsurface inflow to the GC by the peninsula side and an outflow by the continental side (Fig. 10A&C), forcing the OMZ-core out of the GC mouth along the mainland side. Our results suggest that a weaker winter anticyclonic eddy is also formed at the GC mouth (Fig. 10A) and could be responsible for the weak deepening of the OMZ-top and the less-pronounced contraction of the OMZ-core in February and March (Fig. 6). Contrarily, the winter wind acts in the opposite way, shoaling the OMZ-top by the influence of wind stress curl and wind-induced coastal upwelling (Lavín and Marinone, 2003; Zamudio et al., 2008).

North of 26 °N the deepening of the OMZ-top during summer is more pronounced, creating a front-like pattern, very likely to be caused by interaction between the oxygenated Gulf of California Water and the poor-oxygenated Subtropical Subsurface Water (Lavín and Marinone, 2003; Trucco-Pignata et al., 2019). While the poleward undercurrent next to the continental border is narrow, the outflow due to the anticyclonic eddy is wider and covers the eastern half of the GC mouth (Fig. 10 & 11). This explains why the isolines of the OMZ-top tend to be aligned with the gulf axis during the expansion periods while they tend to be perpendicular to the gulf's axis during the contraction in summer (Fig. 4).

5.4. Interannual variability

The characteristics of the OMZ boundary during strong El Niño and La Niña events showed marked deviations from the average conditions, mainly in winter (JFM). Most of the differences were related to changes in the subsurface dynamics that dominate the seasonal patterns, i.e., the semiannual poleward undercurrent and the anticyclonic circulation at the SGC.

During La Niña 2010–2011, the OMZ-top was slightly shallower than average, and the OMZ-core reached ~1° farther north inside the GC, both in fall and winter (Fig. 8). However, the poleward undercurrent, responsible for advecting the OMZ-core inside the GC, was not stronger than average, so the OMZ position difference was not caused by an enhanced poleward flow (Fig. 12A, B). During La Niña 2010–11, a sequence of upwelling CTWs reached the GC (Fig. 9B) which could cause the observed intensification in the anticyclonic eddy in the SGC (S8A,C). However, this eddy was shallow (~100 m depth) (Fig. 12D), so neither participated in the contraction of the OMZ-core. Furthermore, during the previous summer (2010), the subsurface circulation at the GCE, including the anticyclonic eddy in the mouth, was weaker than average (not shown). Therefore, the OMZ-core expulsion from the GC by this eddy was also weaker, so when the following expansion period in winter started, the OMZ-core was already closer to the GC mouth.

El Niño affects the GC by i) propagating downwelling CTWs, ii) decreasing upwelling favorable winds, and iii) enhancing the advection of Tropical Surface Water to the north (Herrera-Cervantes et al., 2007; Lluch-Cota et al., 2010). El Niño 2015–16 was one of the strongest events recorded and was preceded by an anomalous warm episode in 2014–2015 (Sanchez-Cabeza et al., 2022). The model showed a period of propagation of downwelling CTWs, which started in 2014, intensified during fall-winter 2015–16 and coincided with deepening periods of the OMZ-top. The observed peak of shared energy (period ~55 days) in the SLA and OMZ-top cross-spectrum agrees with the time scales of

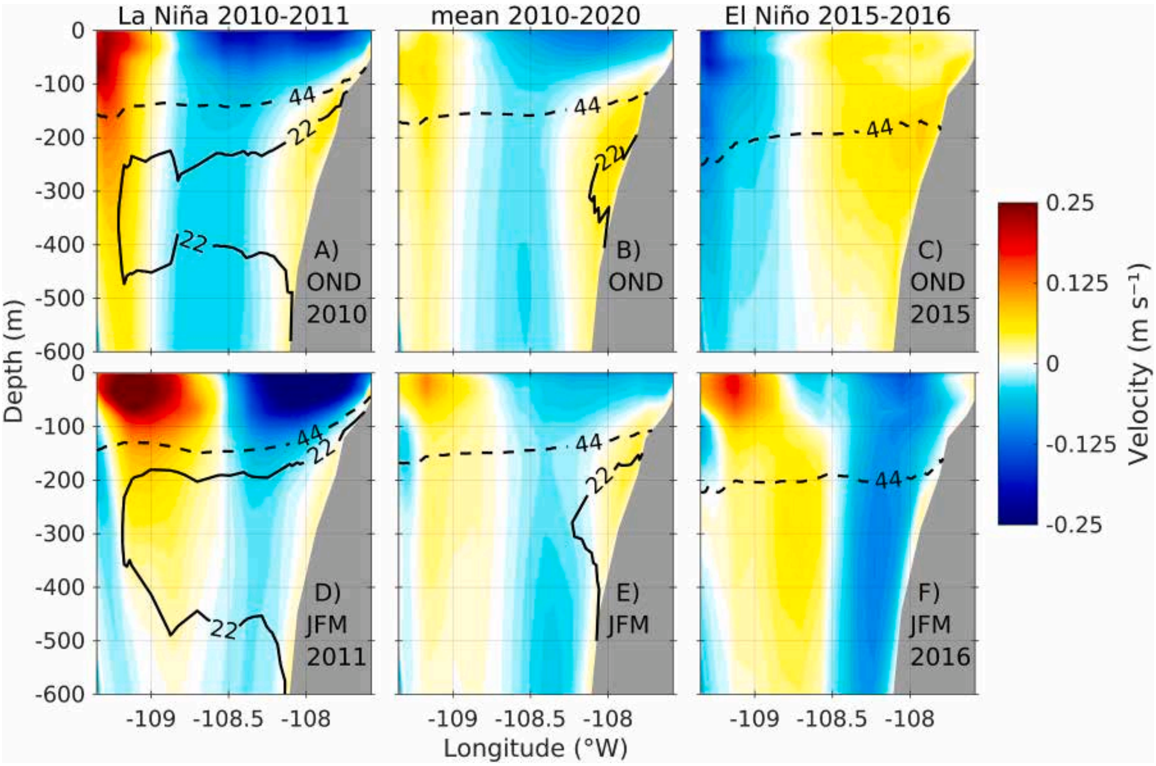

Fig. 12. Comparison of the transect of the velocity perpendicular to the GC mouth during OND (upper panel) and JFM (lower panel) of La Niña 2010–2011 (left column), mean over the 2010 – 2020 period (middle column) and El Niño 2015–2016 events (right column).

equatorially-forced CTWs (Spillane et al., 1987; Gutiérrez et al., 2014) and suggests that the deepening during El Niño is associated with the passage of CTWs. However, north of Cabo Corrientes, inside the GCE (23 °N), the peak in the cross-spectrum disappeared, even though the propagation of CTWs continued (Fig. 9). As the OMZ-top was deeper in this area (GCE), it may have been less sensitive to the dominant CTWs low-order modes. Furthermore, the CGE is a transition area where other processes, such as mesoscale eddies and the presence of water masses with different properties, may influence the variability of OMZ-top.

The substantial variability of the OMZ boundary modelled in the GCE during El Niño 2015–16 appears to be related to an intensification of mesoscale dynamics (Figs. S8B, D). During OND 2015, there was an intensification in the poleward flow next to the coast, which was broad and covered the eastern half of the GC mouth. Since the intensification was not reproduced in the LFBRY simulation, it is expected that it was enhanced by the arrival of downwelling CTWs (Zamudio et al., 2008; Gómez-Valdivia et al., 2015). However, owing to the deepening of the isotherms associated with El Niño, the enhanced poleward advection of warm, oxygenated Tropical Surface Water rather than oxygen-depleted Subtropical Subsurface Water took place (Fig. 12C) (Castro et al., 2000). Later, in winter 2016, the anticyclonic circulation in the GC mouth was much stronger than average (Fig. 12, Fig. S8), causing the expulsion of the OMZ-core far more southern than the GC mouth. The OMZ boundary in the El Niño 2015–16 winter was comparable to an average summer (Fig. 8). This intensification was not reproduced in the sensitivity experiment (LFBRY), suggesting that the CTWs associated with El Niño enhanced the poleward flow related to the intensity of the anticyclonic circulation in the GCE (Gómez-Valdivia et al., 2015; Farach-Espinoza et al., 2021). El Niño events are also associated with weakening upwelling favorable winds (Herrera-Cervantes et al., 2007; Farach-Espinoza et al.,2021). However, the wind stress estimated by the model showed an increase of up to 40 % of wind stress in the upper mid-GC during the 2015 fall (OND), while in JFM there was a slight decrease (< 10 %) of the wind stress in the lower middle GC (not shown). Therefore, it is not expected that the OMZ-top differences could be related to differences in the upwelling rate.

5.5. *Model limitations and future work*

Our study utilizes the CROCO-PISCES coupled physical-biogeochemical model with a horizontal resolution of approximately 9 km to investigate the seasonal and interannual variability of the OMZ at the Gulf of California Entrance (GCE). The purpose of the model was to gain a better understanding of OMZ variability, where observational data are very scarce. While the model effectively captures large-scale dynamical processes (such as mesoscale eddies, poleward undercurrents, and coastal-trapped waves), it is subject to limitations that can lead to some discrepancies with observations.

In this work, both the validation and discussion focus on the Gulf of California area, in particular the entrance and the southern part. We validated the model against available datasets, including ARGO float profiles, cruise data from June 2015, and satellite observations (e.g., OSTIA SST and AVISO SLA). These comparisons demonstrate that the model accurately reproduces the general patterns of OMZ variability, including seasonal shoaling and deepening, as well as interannual responses to ENSO. However, the modeled oxycline is somewhat deeper and more diffuse than observed, with a mean depth difference of ~17 m compared to ARGO profiles. This bias could be more pronounced in areas such as the Gulf of California, where observational data are sparse, limiting our ability to assess model performance locally.

Despite this limitation, the model successfully reproduces spatial and temporal patterns of OMZ variability driven by physical processes. For instance, it accurately captures the latitudinal patterns of the OMZ boundary, such as the front-like structure around 24 °N observed in the June 2015 cruise data (Figs. S4 and S5), which is associated with mesoscale eddy activity. The model also reproduces the semiannual cycle of OMZ-top shoaling and deepening, as well as the poleward expansion/contraction of the OMZ-core (Figs. 5 and 6), aligning with known dynamical processes, such as the Mexican Coastal Current and the anticyclonic eddy in the GCE during summer. These results suggest that, while the model exhibits a vertical bias in oxygen distribution, it provides a robust framework for understanding the physical drivers of OMZ variability, particularly in data-scarce regions. Possible reasons for discrepancies on the OMZ depth could be:

- Model spatial resolution limitations: The 9 km horizontal resolution may not adequately resolve fine-scale processes that significantly influence OMZ depths in the GC. Small-scale dynamics are critical in shaping oxygen distributions in coastal regions and may not be fully captured at this resolution.
- Parameterization of Biogeochemical Processes: The model's parameterization of biogeochemical processes (via PISCES) relies on generalized assumptions that may not be optimally tuned for the unique conditions of the GC. For instance, the simulation of oxygen consumption through microbial respiration may differ from reality due to region-specific characteristics that are not fully accounted for in the default parameter settings.

These discrepancies highlight the challenges inherent in ocean modeling, particularly in regions with complex coastal dynamics and limited observational coverage. To improve the model's representation of OMZ depths in future work, we propose the following:

- Higher-resolution simulations: Increasing the horizontal and vertical resolution could better capture small-scale processes, such as localized upwelling, (sub)mesoscale fronts and eddies, and topographic effects, potentially reducing the observed differences in OMZ depth.
- Region-specific parameter tuning: Adjusting the parameterization of biogeochemical processes based on additional regional data could enhance the model's accuracy for the GC.
- Expanded observational data: The scarcity of in situ measurements, such as biogeochemical ARGO floats in the Gulf of California, limits validation efforts. Future deployment of such instruments in the region would provide critical data to refine and validate the model.

An Empirical Orthogonal Function (EOF) analysis of the OMZ-top and core could deepen our understanding of the variability modes associated with El Niño and La Niña events. This analysis would complement our current findings, which demonstrate the significant impact of El Niño (deepening and contraction of the OMZ) and La Niña (shoaling and expansion) through seasonal and interannual comparisons (e.g., Figs. 7, 8, and 9). Additionally, the results could help disentangle ENSO-driven variability from other modes of variability in the OMZ.

Besides the influence of dynamic processes on the OMZ boundary variability in the GCE, other processes, particularly biogeochemical, could also be relevant. Regarding interannual variability, El Niño events typically decrease primary productivity, while La Niña events increase it (Kahru et al., 2004; Lluch-Cota et al., 2010). These changes in primary production are expected to contribute to OMZ-top deepening or shoaling of the OMZ-top. The discussion of the biogeochemical processes involved is beyond the scope of this work and is deferred to future work. In any case, our model, despite its limitations, provides valuable insights into the drivers of OMZ variability in the GCE and serves as a foundation for further research.

6. Conclusions

This study highlights the dynamic behavior of the oxygen minimum zone boundary (OMZ) at the Gulf of California entrance (GCE), revealing distinct patterns of shoaling and deepening influenced by various oceanographic processes. The seasonal variability exhibits a semiannual cycle of alternate periods of shoaling and deepening of the OMZ boundary, significantly influenced by seasonal shifts of a poleward undercurrent along the coast and the following formation of an anticyclonic eddy within the GC mouth. The poleward undercurrent, which is part of the Mexican Coastal Current, shoals the OMZ upper limit and pushes the OMZ core to the GC during fall and spring. The anticyclonic eddy, occurring in winter (weaker) and summer, deepens the OMZ upper limit and forces the OMZ core out of the gulf by the continental side. The interaction between local mesoscale dynamics and remote forcings, particularly coastal-trapped waves (CTWs), plays a significant role in shaping the OMZ boundary's behavior. The study confirms that while CTWs enhance the poleward flow and intensify the anticyclonic circulation, their absence does not prevent the formation of anticyclonic eddies at the Gulf's entrance.

Interannual variability, particularly during strong El Niño and La Niña events, shows the OMZ boundary's sensitivity to changes in oceanic and atmospheric conditions. El Niño events lead to a pronounced deepening of the OMZ, driven by enhanced mesoscale activity. In contrast, La Niña events cause a shoaling effect, intensifying the OMZ's presence along the coast.

This research demonstrates the value of integrating high-resolution ocean models with observational data to unravel the complex interplay between physical and biogeochemical processes driving the OMZ variability, especially in regions with limited observational data availability. Future work should further explore the role of biogeochemical processes in OMZ dynamics, particularly under changing climatic conditions.

CRediT authorship contribution statement

Carlos Alberto Herrera-Becerril: Writing – review & editing, Writing – original draft, Software, Formal analysis, Conceptualization. **François Colas:** Writing – review & editing, Writing – original draft, Supervision, Software, Resources, Funding acquisition, Formal analysis, Conceptualization. **Sanchez-Cabeza Joan Albert:** Writing – review & editing, Writing – original draft, Supervision, Resources, Funding acquisition, Formal analysis, Conceptualization. **José Martín Hernández-Ayón:** Writing – review & editing, Writing – original draft, Supervision. **Vincent Echevin:** Writing – review & editing, Writing – original draft, Supervision. **José Gilberto Cardoso-Mohedano:** Writing – review & editing, Writing – original draft, Supervision, Software. **Ana Carolina Ruiz-Fernández:** Writing – review & editing, Writing – original draft, Resources, Funding acquisition.

Funding sources

The numerical simulations were performed on the IDRIS Jean-Zay high performance computers under DARI projects A0130101140 and A0110101140. This work was also funded by Universidad Nacional Autónoma de México (UNAM, projects PAPIIT IB201612, IN110518, IN103721and IN110624), CONAHCYT (PDCPN 214349 and SEMARNAT 278634), the International Atomic Energy Agency (Technical cooperation projects RLA7020, RLA7022, RLA7025 and RLA7028). The collaboration between UNAM and IRD is through the IRN DEXICOTROP project. Support by i) the Posgrado en Ciencias del Mar y Limnología, UNAM, ii) Sorbonne Université, École doctorale 129, Sciences de l'Environnement d'Ile de France, iii) Campus France, and a PhD fellowship from CONAHCYT (CVU No. 823599) is acknowledged by Carlos Alberto Herrera-Becerril.

Declaration of Competing Interest

The authors declare that they have no known competing financial interests or personal relationships that could have appeared to influence the work reported in this paper.

Acknowledgments

We acknowledge Support by CONACyT through projects

PDCPN2013–01/ 214349 and CONACyT SEMARNAT-2016–01–278634. Cruise data from June 2015 was supported by the project lead by Laura Sánchez-Velasco (2014–236864) “Influencia de remolinos de mesoescala sobre hábitats de larvas de peces (con énfasis en especies de importancia comercial) en la zona de mínimo de oxígeno del océano Pacífico frente a México: Océano abierto y efecto de islas,” the project SEP – CONACyT (#2011–168034-T) “Un estudio de la Corriente Costera Mexicana y el Pacífico adyacente, con un ‘SeaGlider,’ cruceros oceanográficos y datos de satélite,” and the project CONACyT Fronteras de la Ciencia 180 “Probando paradigmas sobre la expansión de la zona de mínimo de oxígeno: reducción del hábitat vertical del zooplancton y su efecto en el ecosistema pelágico mediante métodos autónomos”. The long-term project Coastal Observatories of Global Change would not be possible without the institutional support received by the Direction and Administration of the Instituto de Ciencias del Mar y Limnología, UNAM, through the years at the Mazatlán observatory (including the project Pandemia Covid-19 (2020) Cero Turismo) and the PAPIIT-UNAM programme (projects IN110624, IN103721 and IN110518). The authors thank the technical support provided by Benjamín Yáñez Chávez, Beatriz Yáñez Rivera and Sergio Rendón Rodríguez† (sampling), Marcela Guillermina Fregoso López, and Libia Hascibe Pérez Bernal (laboratory analysis), Carlos Suárez Gutiérrez and León Felipe Álvarez Sánchez (data management).

Appendix A. Supporting information

Supplementary data associated with this article can be found in the online version at doi:10.1016/j.rsma.2025.104399.

Data Availability

Data will be made available on request. The CROCO-PISCES model is open-source and freely available at https://www.croco-ocean.org/. Model outputs are very large and will be made available on request to the corresponding author.

References

Auger, P.A., Bento, J.P., Hormazabal, S., Morales, C.E., Bustamante, A., 2021. Mesoscale variability in the boundaries of the oxygen minimum zone in the eastern south pacific: influence of intrathermocline eddies. J. Geophys. Res. Oceans 126 (2), e2019JC015272. https://doi.org/10.1029/2019JC015272.

Aumont, O., Bopp, L., 2006. Globalizing results from ocean in situ iron fertilization studies. Glob. Biogeochem. Cycles 20 (2). https://doi.org/10.1029/2005GB002591.

Aumont, O., Éthé, C., Tagliabue, A., Bopp, L., Gehlen, M., 2015. PISCES-v2: an ocean biogeochemical model for carbon and ecosystem studies. Geosci. Model Dev. 8 (2), 2465–2513. https://doi.org/10.5194/gmd-8-2465-2015.

Bange, H.W., 2008. Gaseous nitrogen compounds (NO, N_2O, N_2, NH_3) in the ocean. In: Capone, D.G., Bronk, D.A., Mulholland, M.R., Carpenter, E.J. (Eds.), Nitrogen in the Marine Environment, Second ed. Elsevier, pp. 51–94. B978-0-12-372522-6.00021-9.

Boening, C., Willis, J.K., Landerer, F.W., Nerem, R.S., Fasullo, J., 2012. The 2011 la Niña: so strong, the oceans fell. Geophys. Res. Lett. 39 (19). https://doi.org/10.1029/2012GL053055.

Boyer, T.P., Antonov, J.I., Baranova, O.K., Garcia, H.E., Johnson, D.R., Locarnini, R.A., Mishonov, A.V., D. O’Brien, T., Seidov, D., Smolyar, I.V., Zweng, M.M., 2009. In: Levitus, S. (Ed.), World Ocean Database 2009, NOAA Atlas NESDIS, 66. U.S. Gov. Printing Office, Washington, D.C., p. 219. ⟨https://www.ncei.noaa.gov/products/world-ocean-database⟩ (DVDs).

Brandt, P., Bange, H.W., Banyte, D., Dengler, M., Didwischus, S.-H., Fischer, T., Greatbatch, R.J., Hahn, J., Kanzow, T., Karstensen, J., Körtzinger, A., Krahmann, G., Schmidtko, S., Stramma, L., Tanhua, T., Visbeck, M., 2015. On the role of circulation and mixing in the ventilation of oxygen minimum zones with a focus on the eastern tropical north atlantic. Biogeosciences 12 (2), 489–512. https://doi.org/10.5194/bg-12-489-2015.

Bretagnon, M., Paulmier, A., Garçon, V., Dewitte, B., Illig, S., Leblond, N., Coppola, L., Campos, F., Velazco, F., Panagiotopoulos, C., Oschlies, A., Hernandez-Ayon, J.M., Maske, H., Vergara, O., Montes, I., Martinez, P., Carrasco, E., Grelet, J., Desprez-De-Gesincourt, O., Maes, C., Scouarnec, L., 2018. Modulation of the vertical particle transfer efficiency in the oxygen minimum zone off Peru. Biogeosciences 15 (16), 5093–5111. https://doi.org/10.5194/bg-15-5093-2018.

Castro, R., Mascarenhas, A.S., Durazo, R., Collins, C.A., 2000. Variación estacional de la temperatura y salinidad en la entrada del golfo de california, México. Cienc. Mar. 26 (4), 561–583. https://doi.org/10.7773/cm.v26i4.621.

Cepeda-Morales, J., Gaxiola-Castro, G., Beier, E., Godínez, V.M., 2013. The mechanisms involved in defining the Northern boundary of the shallow oxygen minimum zone in the eastern tropical Pacific Ocean off Mexico. Deep Sea Res. Part I Oceanogr. Res. Pap. 76, 1–12. https://doi.org/10.1016/j.dsr.2013.02.004.

Claustre, H., Johnson, K.S., Takeshita, Y., 2020. Observing the global ocean with biogeochemical-Argo. Annu. Rev. Mar. Sci. 12, 23–48. https://doi.org/10.1146/annurev-marine-010419-010956.

Copernicus marine service information (CMEMS), 2023. Global Ocean Physics Reanalysis, E.U.Mar. Data Store (MDS). Accessed on 08 Feb 2025. https://doi:.org/10.48670/moi-00021.

Delgadillo-Hinojosa, F., Segovia-Zavala, J.A., Huerta-Díaz, M.A., Atilano-Silva, H., 2006. Influence of geochemical and physical processes on the vertical distribution of manganese in Gulf of California waters. Deep Sea Res. Part I Oceanogr. Res. Pap. 53 (8), 1301–1319. https://doi.org/10.1016/j.dsr.2006.05.008.

Devol, A.H., Uhlenhopp, A.G., Naqvi, S.W.A., Brandes, J.A., Jayakumar, D.A., Naik, H., Gaurin, S., Codispoti, L.A., Yoshinari, T., 2006. Denitrification rates and excess nitrogen gas concentrations in the Arabian Sea oxygen deficient zone. Deep Sea Res. Part I Oceanogr. Res. Pap. 53 (9), 1533–1547. https://doi.org/10.1016/j.dsr.2006.07.005.

Diaz, R.J., Rosenberg, R., 2008. Spreading dead zones and consequences for marine ecosystems. Science 321 (5891), 926–929. https://doi.org/10.1126/science.1156401.

Espinoza-Morriberón, D., Echevin, V., Colas, F., Tam, J., Gutiérrez, D., Graco, M., Ledesma, J., Quispe-Ccalluari, C., 2019. Oxygen variability during ENSO in the tropical south eastern pacific. Front. Mar. Sci. 5, 526. https://doi.org/10.3389/fmars.2018.00526.

Fairall, C. W., Bradley, E. F., Hare, J. E., Grachev, A. A., & Edson, J. B. (2003). Bulk parameterization of air–sea fluxes: Updates and verification for the COARE algorithm. Journal of climate, 16(4), 571-591. https://doi.org/10.1175/1520-0442(2003)016%3C0571:BPOASF%3E2.0.CO;2.

Farach-Espinoza, E.B., López-Martínez, J., García-Morales, R., Nevárez-Martínez, M.O., Lluch-Cota, D.B., Ortega-García, S., 2021. Temporal variability of oceanic mesoscale events in the Gulf of California. Remote Sens. 13 (9), 1774. https://doi.org/10.3390/rs13091774.

Färber-Lorda, J.F., Färber-Data, B.F., 2023. Autumn vertical distribution of zooplankton in the oxygen minimum zone of the eastern tropical north pacific. Mar. Environ. Res. 190, 106116. https://doi.org/10.1016/j.marenvres.2023.106116.

Fernández-Álamo, M.A., Färber-Lorda, J., 2006. Zooplankton and the oceanography of the eastern tropical pacific: a review. Prog. Oceanogr. 69 (2-4), 318–359. https://doi.org/10.1016/j.pocean.2006.03.003.

Flores-Vidal, X., Durazo, R., Zavala-Sansón, L., Flament, P., Chavanne, C., Ocampo-Torres, F.J., Reyes-Hernández, C., 2014. Evidence of inertially generated coastal-trapped waves in the eastern tropical pacific. J. Geophys. Res. Oceans 119 (5), 3121–3133. https://doi.org/10.1002/2013JC009118.

Fuenzalida, R., Schneider, W., Garcés-Vargas, J., Bravo, L., Lange, C., 2009. Vertical and horizontal extension of the oxygen minimum zone in the eastern south Pacific Ocean. Deep Sea Res. Part II Top. Stud. Oceanogr. 56 (16), 992–1003. https://doi.org/10.1016/j.dsr2.2008.11.001.

Gallo, N.D., Levin, L.A., 2016. Fish ecology and evolution in the world’s oxygen minimum zones and implications of ocean deoxygenation. Adv. Mar. Biol. 74, 117–198. https://doi.org/10.1016/bs.amb.2016.04.001.

Garcia, H.E., Wang, Z., Bouchard, C., Cross, S.L., Paver, C.R., Reagan, J.R., Boyer, T.P., Locarnini, R.A., Mishonov, A.V., Baranova, O., Seidov, D., Dukhovskoy, D., 2024. World ocean Atlas 2023, volume 3: dissolved oxygen, apparent oxygen utilization, and oxygen saturation. A. Mishonov Tech. Ed. NOAA Atlas NESDIS 91. https://doi.org/10.25923/rb67-ns53.

Godínez, V.M., Beier, E., Lavín, M.F., Kurczyn, J.A., 2010. Circulation at the entrance of the Gulf of California from satellite altimeter and hydrographic observations. J. Geophys. Res. Oceans 115 (C4). https://doi.org/10.1029/2009JC005705.

Gómez-Valdivia, F., Parés-Sierra, A., Flores-Morales, A.L., 2015. The Mexican coastal current: a subsurface seasonal bridge that connects the tropical and subtropical northeastern pacific. Cont. Shelf Res. 110, 100–107. https://doi.org/10.1016/j.csr.2015.10.010.

Good, S., Fiedler, E., Mao, C., Martin, M.J., Maycock, A., Reid, R., Roberts-Jones, J., Searle, T., Waters, J., While, J., Worsfold, M., 2020. The current configuration of the OSTIA system for operational production of foundation sea surface temperature and ice concentration analyses. Remote Sens 12, 720. https://doi.org/10.3390/rs12040720.

Gutiérrez, M.O., López, M., Candela, J., Castro, R., Mascarenhas, A., Collins, C.A., 2014. Effect of coastal-trapped waves and wind on currents and transport in the Gulf of California. J. Geophys. Res. Oceans 119 (8), 5123–5139. https://doi.org/10.1002/2013JC009538.

Helly, J.J., Levin, L.A., 2004. Global distribution of naturally occurring marine hypoxia on continental margins. Deep Sea Res. Part I Oceanogr. Res. Pap. 51 (9), 1159–1168. https://doi.org/10.1016/j.dsr.2004.03.009.

Herrera-Becerril, C.A., Sanchez-Cabeza, J.A., Sánchez, L.F.Á., Lara-Cera, A.R., Ruiz-Fernández, A.C., Cardoso-Mohedano, J.G., Colas, F., 2022. Statistical identification of coastal hypoxia events controlled by wind-induced upwelling. Cont. Shelf Res. 233, 104634. https://doi.org/10.1016/j.csr.2021.104634.

Herrera-Cervantes, H., Lluch-Cota, D.B., Lluch-Cota, S.E., Gutiérrez-de-Velasco S, G., 2007. The ENSO signature in sea-surface temperature in the Gulf of California. J. Mar. Res. 65 (5), 589–605. https://doi.org/10.1357/002224007783649529.

Hersbach, H., Bell, B., Berrisford, P., Biavati, G., Horányi, A., Muñoz Sabater, J., Nicolas, J., Peubey, C., Radu, R., Rozum, I., Schepers, D., Simmons, A., Soci, C., Dee, D., Thépaut, J.-N. (2018): ERA5 hourly data on single levels from 1979 to present.

Copernicus Climate Change Service (C3S) Climate Data Store (CDS). https://doi.org/10.24381/cds.adbb2d47.

Hilt, M., Roblou, L., Nguyen, C., Marchesiello, P., Lemari e, F., Jullien, S., Dumas, F., Debreu, L., Capet, X., Bordois, L., Benshila, R., Auclair, F., 2020. Numerical modeling of hydraulic control, solitary waves and primary instabilities in the strait of Gibraltar. Ocean Model 151 (16p), 101642. https://doi.org/10.1016/j.ocemod.2020.101642.

Hofmann, A.F., Peltzer, E.T., Walz, P.M., Brewer, P.G., 2011. Hypoxia by degrees: establishing definitions for a changing ocean. Deep Sea Res. Part I Oceanogr. Res. Pap. 58 (12), 1212–1226. https://doi.org/10.1016/j.dsr.2011.09.004.

Kahru, M., Marinone, S.G., Lluch-Cota, S.E., Parés-Sierra, A., Mitchell, B.G., 2004. Ocean-color variability in the Gulf of California: scales from days to ENSO. Deep Sea Res. Part II Top. Stud. Oceanogr. 51 (1-3), 139–146. https://doi.org/10.1016/j.dsr2.2003.04.001.

Kalvelage, T., Lavik, G., Jensen, M.M., Revsbech, N.P., Löscher, C., Schunck, H., Desai, D., Hauss, H., Kiko, R., Holtappels, M., LaRoche, J., Schmitz, R.A., Graco, M.I., Kuypers, M.M., 2015. Aerobic microbial respiration in oceanic oxygen minimum zones. PLOS ONE 10 (7), e0133526. https://doi.org/10.1371/journal.pone.0133526.

Karstensen, J., Stramma, L., Visbeck, M., 2008. Oxygen minimum zones in the eastern tropical atlantic and pacific oceans. Prog. Oceanogr. 77 (4), 331–350. https://doi.org/10.1016/j.pocean.2007.05.009.

Kessler, W.S., 2006. The circulation of the eastern tropical pacific: a review. Prog. Oceanogr. 69 (2-4), 181–217. https://doi.org/10.1016/j.pocean.2006.03.009.

Key, R.M., Kozyr, A., Sabine, C.L., Lee, K., Wanninkhof, R., Bullister, J.L., Feely, R.A., Millero, F.J., Mordy, C., Peng, T.H., 2004. A global ocean carbon climatology: results from global data analysis project (GLODAP). Glob. Biogeochem. Cycles 18 (4). https://doi.org/10.1029/2004GB002247.

Kurczyn, J.A., Beier, E., Lavín, M.F., Chaigneau, A., 2012. Mesoscale eddies in the northeastern pacific tropical-subtropical transition zone: statistical characterization from satellite altimetry. J. Geophys. Res. Oceans 117 (C10). https://doi.org/10.1029/2012JC007970.

Large, W.G., McWilliams, J.C., Doney, S.C., 1994. Oceanic vertical mixing: a review and a model with a nonlocal boundary layer parameterization. Rev. Geophys. 32 (4), 363–403. https://doi.org/10.1029/94RG01872.

Lavín, M.F., Castro, R., Beier, E., Godínez, V.M., Amador, A., Guest, P., 2009. SST, thermohaline structure, and circulation in the Southern Gulf of California in June 2004 during the north American monsoon experiment. J. Geophys. Res. Oceans 114 (C2). https://doi.org/10.1029/2008JC004896.

Lavín, M.F., Castro, R., Beier, E., Godínez, V.M., 2013. Mesoscale eddies in the Southern Gulf of California during summer: characteristics and interaction with the wind stress. J. Geophys. Res. Oceans 118 (3), 1367–1381. https://doi.org/10.1002/jgrc.20132.

Lavín, M.F., Marinone, S.G., 2003. An overview of the physical oceanography of the Gulf of California. Nonlinear Process. Geophys. Fluid Dyn. A Tribut. Sci. Work Pedro Ripa 173–204. https://doi.org/10.1007/978-94-010-0074-1_11.

Lemarié, F., Kurian, J., Shchepetkin, A.F., Molemaker, M.J., Colas, F., McWilliams, J.C., 2012. Are there inescapable issues prohibiting the use of terrain-following coordinates in climate models? Ocean Model. 42, 57–79. https://doi.org/10.1016/j.ocemod.2011.11.007.

Liang, J.H., McWilliams, J.C., Kurian, J., Colas, F., Wang, P., Uchiyama, Y., 2012. Mesoscale variability in the northeastern tropical pacific: forcing mechanisms and eddy properties. J. Geophys. Res. Oceans 117 (C7). https://doi.org/10.1029/2012JC008008.

Lluch-Cota, S.E., Parés-Sierra, A., Magaña-Rueda, V.O., Arreguín-Sánchez, F., Bazzino, G., Herrera-Cervantes, H., Lluch-Belda, D., 2010. Changing climate in the Gulf of California. Prog. Oceanogr. 87 (1-4), 114–126. https://doi.org/10.1016/j.pocean.2010.09.007.

Márquez-Artavia, A., Sánchez-Velasco, L., Barton, E.D., Paulmier, A., Santamaría-Del-Ángel, E., Beier, E., 2019. A suboxic chlorophyll-a maximum persists within the pacific oxygen minimum zone off Mexico. Deep Sea Res. Part II Top. Stud. Oceanogr. 169, 104686. https://doi.org/10.1016/j.dsr2.2019.104686.

McCoy, D., Damien, P., Clements, D., Yang, S., Bianchi, D., 2023. Pathways of nitrous oxide production in the eastern tropical south pacific oxygen minimum zone. Glob. Biogeochem. Cycles 37 (7), e2022GB007670. https://doi.org/10.1029/2022GB007670.

Páez-Osuna, F., Sanchez-Cabeza, J.A., Ruiz-Fernández, A.C., Alonso-Rodríguez, R., Piñón-Gimate, A., Cardoso-Mohedano, J., Flores-Verdugo, F., Carballo, J.L., Cisneros-Mata, M.Á., Álvarez-Borrego, S., 2016. Environmental status of the Gulf of California: a review of responses to climate change and climate variability. EarthSci. Rev. 162, 253–268. https://doi.org/10.1016/j.earscirev.2016.09.015.

Pantoja, D.A., Marinone, S.G., Parés-Sierra, A., Gómez-Valdivia, F., 2012. Modelación numérica de la hidrografía y circulación estacional y de mesoescala en el Pacífico central mexicano. Cienc. Mar. 38 (2), 363–379. https://doi.org/10.7773/cm.v38i2.2007.

Paulmier, A., Ruiz-Pino, D., 2009. Oxygen minimum zones (OMZs) in the modern ocean. Prog. Oceanogr. 80 (3-4), 113–128. https://doi.org/10.1016/j.pocean.2008.08.001.

Pegau, W.S., Boss, E., Martínez, A., 2002. Ocean color observations of eddies during the summer in the Gulf of California, 1 Geophys. Res. Lett. 29 (9), 6. https://doi.org/10.1029/2001GL014076.

Penven, P., Cambon, G., Marchesiello, P., Sepulveda, A., Benshila, R., Illig, S., Jullien, S., Le Gentil, S., Le Corre, M., Morvan, G., Rougier, G., 2019. Zenodo. CROCO Tools (1.1). https://doi.org/10.5281/zenodo.7432028.

Penven, P., Debreu, L., Marchesiello, P., McWilliams, J.C., 2006. Evaluation and application of the ROMS 1-way embedding procedure to the central california upwelling system. Ocean Model. 12 (1-2), 157–187. https://doi.org/10.1016/j.ocemod.2005.05.002.

Portela, E., Beier, E., Barton, E.D., Castro, R., Godínez, V., Palacios-Hernández, E., Trasviña, A., 2016. Water masses and circulation in the tropical pacific off central Mexico and surrounding areas. J. Phys. Oceanogr. 46 (10), 3069–3081. https://doi.org/10.1175/jpo-d-16-0068.1.

Pujol, M.I., Faugère, Y., Taburet, G., Dupuy, S., Pelloquin, C., Ablain, M., Picot, N., 2016. DUACS DT2014: the new multi-mission altimeter data set reprocessed over 20 years. Ocean Sci. 12 (5), 1067–1090. https://doi.org/10.5194/os-12-1067-2016.

Resplandy, L., Lévy, M., Bopp, L., Echevin, V., Pous, S., Sarma, V.V.S.S., Kumar, D., 2012. Controlling factors of the oxygen balance in the Arabian Sea's OMZ. Biogeosciences 9 (12), 5095–5109. https://doi.org/10.5194/bg-9-5095-2012.

Sanchez-Cabeza, J.A., Herrera-Becerril, C.A., Carballo, J.L., Yáñez, B., Álvarez-Sánchez, L.F., Cardoso-Mohedano, J.G., Ruiz-Fernández, A.C., 2022. Rapid surface water warming and impact of the recent (2013–2016) temperature anomaly in shallow coastal waters at the eastern entrance of the Gulf of California. Prog. Oceanogr. 202, 102746. https://doi.org/10.1016/j.pocean.2022.102746.

Sánchez-Pérez, E.D., Sánchez-Velasco, L., Ruvalcaba-Aroche, E.D., Ornelas-Vargas, A., Beier, E., Barton, E.D., Contreras-Catala, F., 2021. Temperature and dissolved oxygen concentration in the Pacific Ocean at the Northern region of the oxygen minimum zone off Mexico between the last two PDO cool phases. J. Mar. Syst. 222, 103607. https://doi.org/10.1016/j.jmarsys.2021.103607.

Sánchez-Velasco, L., Beier, E., Godínez, V.M., Barton, E.D., Santamaría-del-Angel, E., Jiménez-Rosemberg, S.P.A., Marinone, S.G., 2017. Hydrographic and fish larvae distribution during the "Godzilla el Niño 2015–2016" in the Northern end of the shallow oxygen minimum zone of the eastern tropical Pacific Ocean. J. Geophys. Res. Oceans 122 (3), 2156–2170. https://doi.org/10.1002/2016JC012622.

Shchepetkin, A.F., McWilliams, J.C., 2005. The regional oceanic modeling system (ROMS): a split-explicit, free-surface, topography-following-coordinate oceanic model. Ocean Model. 9 (4), 347–404. https://doi.org/10.1016/j.ocemod.2004.08.002.

Shchepetkin, A.F., McWilliams, J.C., 2009. Computational kernel algorithms for fine-scale, multiprocess, longtime oceanic simulations. In: In Handbook of Numerical Analysis, 14. Elsevier, pp. 121–183. https://doi.org/10.1016/S1570-8659(08)01202-0.

Smith, W.H., Sandwell, D.T., 1997. Global sea floor topography from satellite altimetry and ship depth soundings. Science 277 (5334), 1956–1962. https://doi.org/10.1126/science.277.5334.1956.

Spillane, M.C., Enfield, D.B., Allen, J.S., 1987. Intraseasonal oscillations in sea level along the West Coast of the americas. J. Phys. Oceanogr. 17 (3), 313–325. https://doi.org/10.1175/1520-0485(1987)017<0313:IOISLA>2.0.CO;2.

Stramma, L., Johnson, G.C., Sprintall, J., Mohrholz, V., 2008. Expanding oxygen-minimum zones in the tropical oceans. science 320 (5876), 655–658. https://doi.org/10.1126/science.1153847.

Tegen, I., Fung, I., 1995. Contribution to the atmospheric mineral aerosol load from land surface modification. J. Geophys. Res. Atmosph. 100 (D9), 18707–18726. https://doi.org/10.1029/95JD02051.

Trucco-Pignata, P.N., Hernández-Ayón, J.M., Santamaria-del-Angel, E., Beier, E., Sánchez-Velasco, L., Godínez, V.M., Norzagaray, O., 2019. Ventilation of the upper oxygen minimum zone in the coastal region off Mexico: implications of el Niño 2015–2016. Front. Mar. Sci. 6, 459. https://doi.org/10.3389/fmars.2019.00459.

Vergara, O., Dewitte, B., Montes, I., Garçon, V., Ramos, M., Paulmier, A., Pizarro, O., 2016. Seasonal variability of the oxygen minimum zone off Peru in a high-resolution regional coupled model. Biogeosciences 13 (15), 4389–4410. https://doi.org/10.5194/bg-13-4389-2016.

Ward, B.B., Devol, A.H., Rich, J.J., Chang, B.X., Bulow, S.E., Naik, H., Pratihary, A., Jayakumar, A., 2009. Denitrification as the dominant nitrogen loss process in the Arabian Sea. Nature 461 (7260), 78–81. https://doi.org/10.1038/nature08276.

Willmott, C.J., 1981. On the validation of models. Phys. Geogr. 2 (2), 184–194. https://doi.org/10.1080/02723646.1981.10642213.

Zamudio, L., Hogan, P., Metzger, E.J., 2008. Summer generation of the Southern Gulf of California eddy train. J. Geophys. Res. Oceans 113 (C6). https://doi.org/10.1029/2007JC004467.